Cell Reports

Article

The neuron mixer and its impact on human brain dynamics

Graphical abstract

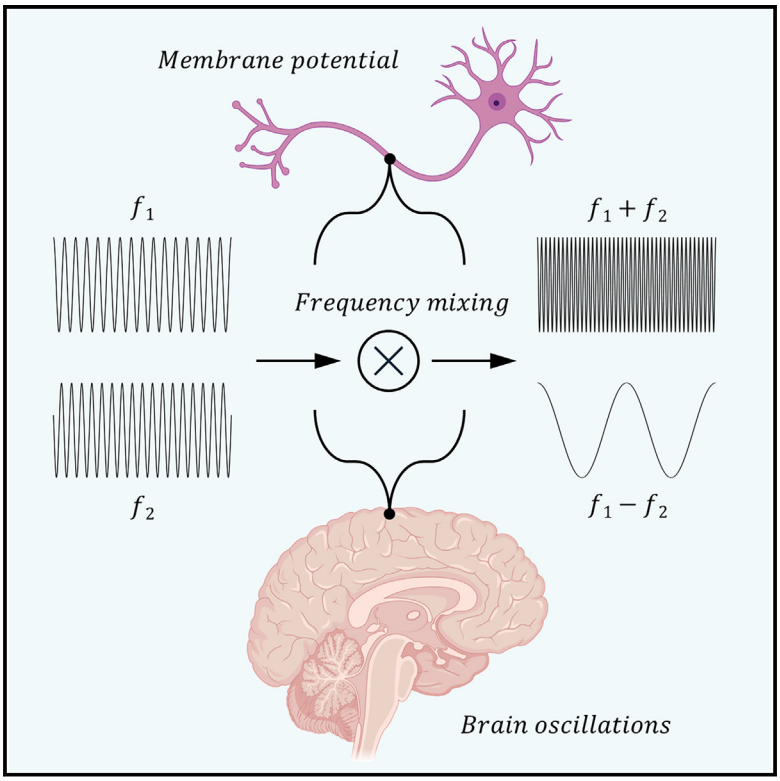

Authors

Charlotte E. Luff, Robert Peach, Emma-Jane Mallas, ..., David J. Sharp, Mauricio Barahona, Nir Grossman

Correspondence

nirg@imperial.ac.uk

In brief

Luff, Peach, et al. demonstrate that the single neuron can act as a signal mixer to create new oscillatory frequencies from exogenous or endogenous subthreshold membrane potential oscillations. They demonstrate that this frequency mixing originates in voltage-gated ion channels and show evidence of functional mixing in the human brain activity.

Highlights

- A single neuron mixes exogenous and endogenous oscillations to produce new frequencies
- Neural frequency mixing originates in the nonlinearity of voltage-gated ion channels
- The human brain EEG displays local and inter-region frequency mixing interactions
- Mixing of human posterior alpha and beta oscillations correlates with visual attention

Luff et al., 2024, Cell Reports *43*, 114274
June 25, 2024
https://doi.org/10.1016/j.celrep.2024.114274

CellPress

Cell Reports

CellPress
OPEN ACCESS

Article

The neuron mixer and its impact on human brain dynamics

Charlotte E. Luff,[1,2,9] Robert Peach,[1,2,3,9] Emma-Jane Mallas,[1,4] Edward Rhodes,[1,2] Felix Laumann,[5] Edward S. Boyden,[6,7] David J. Sharp,[1,4,8] Mauricio Barahona,[5] and Nir Grossman[1,2,10,*]

[1]Department of Brain Sciences, Imperial College London, London, UK
[2]UK Dementia Research Institute, Imperial College London, London, UK
[3]Department of Neurology, University Hospital Würzburg, Würzburg, Germany
[4]UK Dementia Research Institute, Care Research & Technology Centre, London, UK
[5]Department of Mathematics, Imperial College London, London, UK
[6]Department of Brain and Cognitive Sciences, Massachusetts Institute of Technology, Cambridge, MA, USA
[7]Howard Hughes Medical Institute, Chevy Chase, MD, USA
[8]Centre for Injury Studies, Imperial College London, London, UK
[9]These authors contributed equally
[10]Lead contact
*Correspondence: nirg@imperial.ac.uk
https://doi.org/10.1016/j.celrep.2024.114274

SUMMARY

A signal mixer facilitates rich computation, which has been the building block of modern telecommunication. This frequency mixing produces new signals at the sum and difference frequencies of input signals, enabling powerful operations such as heterodyning and multiplexing. Here, we report that a neuron is a signal mixer. We found through *ex vivo* and *in vivo* whole-cell measurements that neurons mix exogenous (controlled) and endogenous (spontaneous) subthreshold membrane potential oscillations, producing new oscillation frequencies, and that neural mixing originates in voltage-gated ion channels. Furthermore, we demonstrate that mixing is evident in human brain activity and is associated with cognitive functions. We found that the human electroencephalogram displays distinct clusters of local and inter-region mixing and that conversion of the salient posterior alpha-beta oscillations into gamma-band oscillations regulates visual attention. Signal mixing may enable individual neurons to sculpt the spectrum of neural circuit oscillations and utilize them for computational operations.

INTRODUCTION

A mixer is a nonlinear device capable of multiplying signals to produce new frequencies, such as the difference and sum of the original input frequencies. A signal mixer made of a transistor, or a diode, has been the building block of modern telecommunication, facilitating the critical conversion to/from higher-frequency bands where transmission efficiency is high (also known as [aka] heterodyning), decoding phase information, and combining multiple signals into one data stream (aka multiplexing).[1,2]

Various neuroscientific studies have reported evidence of a multiplication operation in individual neurons, attributed to their need to implement coincidence detection, i.e., the joint probability of two statistically independent events is the product of probabilities of the individual events.[3] Neural coincidence detection has been observed in diverse tasks, such as the transformation of eye-centric into head-centric coordinates,[4] localization of sound,[5] combination of multisensory signals,[6,7] and detection of visual motion.[8,9] The biophysical underpinning of the multiplication operation has been linked to the nonlinear transfer function of synaptic currents, including log-exp transformation of coincident synaptic excitatory and inhibitory events[10] and concurrent synaptic excitation and release from shunting inhibition events,[11] as well as to the voltage-dependent inactivation of the NMDA receptors.[12,13]

Recent studies have demonstrated the frequency mixing of neural oscillations in rodents' brains (aka signal mixing or spectral mixing but distinct from cross-frequency coupling). Ahrens et al.[14] used local field potential (LFP) recordings in rodents, to show that mechanically evoked neural oscillations in the vibrissae can mix internally, and with spontaneous oscillations induced by anesthesia. Haufler et al.[15] deployed a statistical phase analysis to demonstrate phase dependency between frequency mixing quadruplets (i.e., roots: $f1$, $f2$; products: Δf, $\sum f$) in the spontaneous LFP activity of rodents in a state- and region-dependent manner. Using a computational model, it was proposed that the signal mixing could emerge from individual neurons' nonlinear threshold depolarization characteristics[14,16] (a linear response cannot lead to mixing).

To date, there has not been experimental evidence that an individual neuron can mix transmembrane potentials, and the contribution of this phenomenon to human brain activity has not been explored. Here, we use whole-cell patch clamp

recording in mice to experimentally demonstrate that individual neurons mix exogenous and endogenous transmembrane potential signals and that the signal mixing originates in the nonlinear voltage-gated ion channel currents. Then, we apply phase computation statistics to electroencephalogram (EEG) recordings in human subjects to demonstrate cognitively relevant frequency mixing in the human brain.

RESULTS

Mixing of exogenous membrane potentials in individual neurons

We first examined whether neurons could mix exogenous (controlled) subthreshold membrane oscillations. We applied extracellular sinusoidal electric currents containing two different frequencies (f_1 and f_2), with a difference frequency (Δf) within the normal range of neural activity, and recorded the induced transmembrane potentials in individual neurons *ex vivo* using whole-cell patch clamp recording (Figure 1A). We focused on the subthreshold response of the neurons because suprathreshold spikes at the difference frequency could also be induced by a summation of the applied fields rather than by mixing, i.e., neurons are firing due to polarization at the applied frequencies periodically reaching the action potential threshold. We found that electrical stimulation with two sinusoids at frequencies within the normal range of neural activity (i.e., f_1 = 47 Hz and f_2 = 57 Hz), induced subthreshold membrane potential oscillations at their difference frequency (Δf = 10 Hz) (Figure 1B; note that the stimulation voltages mask the induced subthreshold oscillations at the input frequencies f_1 and f_2).

The induction of a subthreshold membrane oscillation at the difference frequency was consistent across a wide range of stimulation frequencies, spanning three orders of magnitude. Figures 1C and 1D show the subthreshold membrane oscillation induced by electrical stimulation with two sinusoids at frequencies in the upper boundary of neural activity (i.e., f_1 = 497 Hz and f_2 = 507 Hz, Δf = 10 Hz) and far beyond the range of neural activity (i.e., f_1 = 4.997 kHz and f_2 = 5.007 kHz, Δf = 10 Hz) as in temporal interference stimulations,[17,18] respectively. Figure 1E summarizes the induced oscillation amplitude at Δf across this range of applied frequencies (tested against the measurement system's intermodulation distortion [IMD] at Δf[19] i.e., mixing products due to hardware nonlinearity measured in the same way but without brain slices). See Figure S1 for representative unfiltered membrane potential recordings, and Figure S2 for additional membrane potential traces. The amplitude of the induced Δf oscillation was smaller when the stimulation was applied at kHz frequencies. Increasing the amplitude of the applied currents evoked action potential trains at Δf, with a higher current density threshold at kHz frequencies (repeated-measures ANOVA F(5,135) = 22.3, p = 5e−17, Figure 1F). The evocation of frequency mixing products was not exclusive to Δf = 10 Hz. See Figure S3 and Table S3 for subthreshold membrane oscillation induction at Δf = 5 Hz (i.e., f_1 = 47 Hz and f_2 = 52 Hz, f_1 = 4.997 kHz and f_2 = 5.002 kHz) and Δf = 40 Hz (f_1 = 4.997 kHz and f_2 = 5.037 kHz).

The membrane potential power spectra also showed peaks at the sum ($\sum f$) and second harmonics ($2f_1$, $2f_2$) of the applied frequencies (Figures 1Bii, 1Cii, and 1Dii), as predicted by frequency mixing. However, the low membrane oscillation amplitudes at those high frequencies were within the range of the measurement's IMD, rendering these measurements inconclusive, except in the lowest stimulation frequency condition (i.e., f_1 = 7 Hz and f_2 = 17 Hz)—when the induced frequencies were within the range of normal neural activity (i.e., $\sum f$ = 24 Hz, $2f_1$ = 14 Hz, $2f_2$ = 34 Hz). See Figure S2 for all Δf and $\sum f$ membrane potential traces, Figure S4 for statistical comparisons of the sum and harmonic frequencies, Table S1 for a summary of all investigated frequencies, and Tables S2 and S4 for all values and statistics for Figure 1. These results suggest that in addition to the difference frequency, neurons are capable of producing the sum frequency and harmonics of their membrane oscillations. Interestingly, we also found some significant subthreshold membrane oscillations at higher frequency mixing orders, including the second harmonic of the difference frequency (i.e., $2\Delta f$ = 20 Hz; Figure S4D), but not at even higher-order mixings (i.e., $2f_2 - f_1$ and $\sum f - 2\Delta f$; Figures S4E and S4F), suggesting that the neurons are capable of further mixing the mixing products but that the mixing products at higher orders are potentially harder to distinguish from the measurement IMD (see Table S5 for all values and statistics for Figure S4).

Origin of neuronal frequency mixing characterized via pharmacological manipulation

We next explored the cellular origin of the subthreshold signal mixing. We repeated the patch clamp experiment with a subset of the stimulation frequencies and a pharmacological blockade of synaptic input (see STAR Methods for details). We found that blocking the synaptic ion channel currents attenuated, but did not abolish, the Δf oscillation produced by the mixing of frequencies in the normal range of neural activity (i.e., f_1 = 47 Hz and f_2 = 57 Hz) (Figure 2A). Synaptic blockade did not affect the mixing of frequencies beyond the normal neural range (i.e., f_1 = 4.997 kHz and f_2 = 5.007 kHz) (Figure 2B). To exclude the possibility of a confounding contribution from presynaptic neurons driven above threshold at Δf, we repeated the experiment with the same frequencies in the normal range of neural activity but now with the stimulation currents applied intracellularly via the patch pipette to the recorded neurons. We found that the intracellular currents induced subthreshold membrane potential oscillations at their difference frequencies (Figure 2C), confirming the single-cell origin of the subthreshold frequency mixing depolarization. To test whether the frequency mixing is linked to the nonlinearity of the voltage-gated ion channel conductance, we repeated the experiment with a pharmacological blockade of the voltage-gated sodium channels (using tetrodotoxin [TTX]). We found that blocking TTX-sensitive sodium channels suppressed the mixing of membrane oscillations across the tested frequency range (Figures 2D and 2E), implying their involvement in the subthreshold frequency mixing phenomenon (see Table S6 for all values and statistics for Figure 2).

Mixing of endogenous membrane potentials in individual neurons

After confirming that neurons mix exogenous signals, we next examined whether they also mix endogenous (spontaneous)

CellPress
OPEN ACCESS

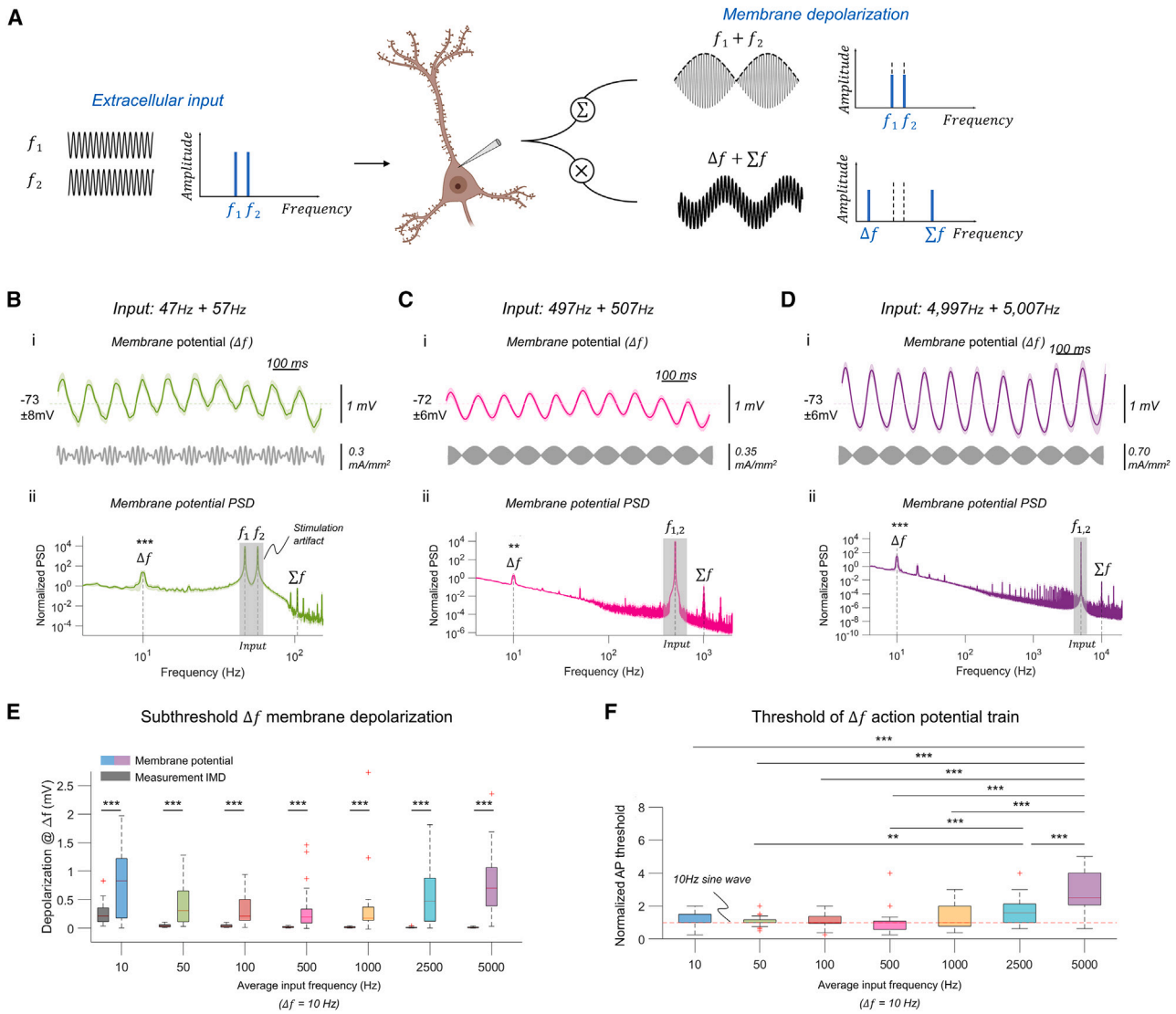

Figure 1. Mixing of exogenous membrane potentials in individual neurons *ex vivo*

(A) Neural mixing concept showing the subthreshold membrane transfer function of multifrequency input with a conventional linear superposition (∑) and the proposed nonlinear mixing via multiplication (X).

(B) (i) Top: neural membrane potential during sinusoidal electrical stimulation with frequencies f_1 = 47 Hz + f_2 = 57 Hz (shown are mean ± SEM). Resting membrane potential mean ± SD is displayed. Raw membrane traces were filtered to remove stimulation artifacts; n = 21 cells. Bottom: applied stimulation current waveform with applied current density mean ± SEM. (ii) Corresponding membrane potential's power spectral density (PSD), mean ± SEM. Raw membrane traces were first filtered to remove offset. PSD values were normalized to endogenous PSD activity at 4 Hz; n = 21 cells. PSD at f_1 and f_2 is dominated by stimulation artifact. ***p < 0.0005, significant PSD peak, one-tailed Wilcoxon signed rank test for zero median.

(C) As in (B) but during stimulation with f_1 = 497 Hz + f_2 = 507 Hz; n = 27 cells. **p < 0.005, one-tailed Wilcoxon signed rank test for zero median.

(D) As in (B) but during stimulation with f_1 = 4,997 Hz + f_2 = 5,007 Hz; n = 29 cells.

(E) Boxplot showing root mean square (RMS) amplitude of the induced neural oscillation at Δf (membrane potential) vs. the measurements' IMD at Δf (measurement IMD) across the range of stimulation frequencies. Traces were first filtered at Δf. RMS values were baseline subtracted. n (IMD/membrane potential) = 20/27 (10 Hz), 20/21 (50 Hz), 25/27 (100 Hz), 26/27 (500 Hz), 21/25 (1,000 Hz), 29/29 (2,500 Hz), 28/29 (5,000 Hz) recordings/cells. ***p < 0.0005, Wilcoxon rank-sum test/two sample t test. Current densities: 0.41 ± 0.31 (10 Hz), 0.30 ± 0.24 (50 Hz), 0.34 ± 0.27 (100 Hz), 0.34 ± 0.22 (500 Hz), 0.33 ± 0.26 (1,000 Hz), 0.45 ± 0.34 (2,500 Hz), 0.69 ± 0.37 (5,000 Hz) mA/mm^2.

(F) Normalized current threshold for action potential (AP) train at Δf across the range of stimulation frequencies. Thresholds were normalized to threshold of a stimulation with 10 Hz sine wave (horizontal red dashed line). * comparisons survived Bonferroni correction (p-value = 0.0071); **p < 0.005 and ***p < 0.0005; repeated-measures ANOVA, post hoc paired t test. Boxplots: central mark, median; box edges, 25th and 75th percentiles; whiskers, extend up to 1.5 × interquartile range box edges; +, datapoints outside this range. n = 22 (10 Hz), 22 (50 Hz), 21 (100 Hz), 21 (500 Hz), 20 (1,000 Hz), 20 (2,500 Hz), and 19 (5,000 Hz) cells.

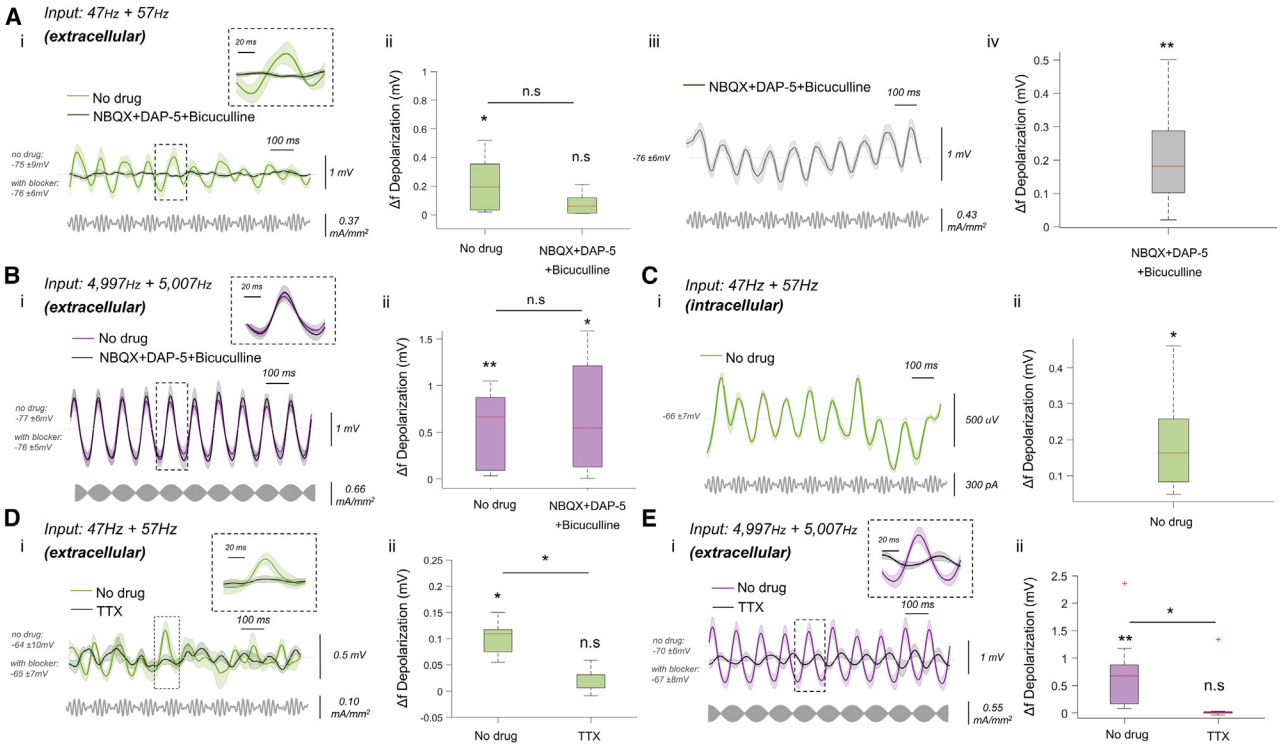

Figure 2. Origin of neuronal mixing characterized via pharmacological manipulation *ex vivo*

(A) (i) Membrane potential during extracellular electrical stimulation with f_1 = 47 Hz + f_2 = 57 Hz, before (color) and during (gray) pharmacological blockade of synaptic NMDA, AMPA, and GABA-A ion channel currents (shown are mean ± SEM). Raw membrane traces were filtered to remove stimulation artifacts. Resting membrane potential mean ± SD is displayed. n = 8 cells. Bottom: applied stimulation current waveform. Zoom view of boxed region at the difference frequency (Δf) is included. (ii) Boxplot of RMS amplitude of the induced neural oscillation at Δf during the stimulation in (i) without drug and with drug. RMS values were baseline-subtracted. (iii and iv) same as (i and ii) but with higher current density stimulation. The asterisk (*) above each box indicates significant oscillation at Δf relative to measurement's IMD at Δf. *p < 0.05 and **p < 0.005, two-sample t test. The asterisk (*) between boxes indicates difference between drug conditions, paired t test. n.s, non-significant. N (IMD/membrane potential) = 8/8 recordings/cells.

(B) As in (Ai) and (Aii) but during stimulation with f_1 = 4,997 Hz + f_2 = 5,007 Hz. n = 9 cells. n (IMD/membrane potential) = 8/9 recordings/cells. *p < 0.05 and **p < 0.005.

(C) As in (Ai) and (Aii) but with intracellular electrical stimulation with f_1 = 47 Hz + f_2 = 57 Hz.

(D) As in (Ai) and (Aii) but before (color) and during (gray) pharmacological blockade of TTX-sensitive conductance. n (IMD/membrane potential) = 7/7 recordings/cells.

(E) As in (D) but during stimulation with f_1 = 4,997 Hz + f_2 = 5,007 Hz. n (IMD/membrane potential) = 11/11 recordings/cells. Boxplots: central mark, median; box edges, 25th and 75th percentiles; whiskers, 1.5× interquartile range; +, datapoints outside this range.

subthreshold membrane potential fluctuations. Subthreshold rhythmic fluctuations are common in neural cells.[20–23] If the membrane potential depolarizes at frequencies f_1 and f_2 ($f_2 > f_1$), and those frequencies are mixed by the membrane, then the instantaneous phases of the frequencies f_1, f_2, and $\Delta f = f_2 - f_1$, must be dependent, i.e., the frequency triplet must show a three-way, but not a pairwise, phase dependency.[15] Similarly, the instantaneous phases of the frequencies within the triplet f_1, f_2, and $\sum f = f_1 + f_2$, the triplet f_1, Δf, and $\sum f$, and the triplet f_2, Δf, and $\sum f$ must also show three-way phase dependencies. Together, the four frequencies comprise a frequency mixing quadruplet. We repeated the *ex vivo* experiment, but now we recorded the transmembrane potentials without electrical stimulation and then assessed the joint phase interaction of all possible frequency mixing quadruplets (i.e., roots: f_1, f_2; products: Δf, $\sum f$) for frequencies within the normal range of neural activity (i.e., up to 250 Hz) using a nonparametric test based on the Lancaster interaction measure[24–26] (Figure 3A; see Figure S5 for sensitivity analysis). The statistical interaction test comprised a three-way interaction measure that was compared against a generated null distribution, which, upon rejection, indicates that the joint probability distribution of the 3 frequency components cannot be factorized (either into pairwise or marginal distributions). To examine the mixing strength, we also defined a heuristic measure of the joint higher-order interaction (JHOI) strength based on the ratio of the interaction measure and the 95% quantile of the null distribution. See STAR Methods for details of the nonparametric test.

We found significant frequency mixing in the spontaneous transmembrane fluctuations of individual neurons spreading across a wide range of root frequency clusters (Figure 3Bi, cluster permutation test computed for each cell individually, see STAR Methods for details). The mixings produced a broad range of new frequencies peaking at the beta and low-gamma bands. Figure 3Bii shows the number of significant mixing interactions

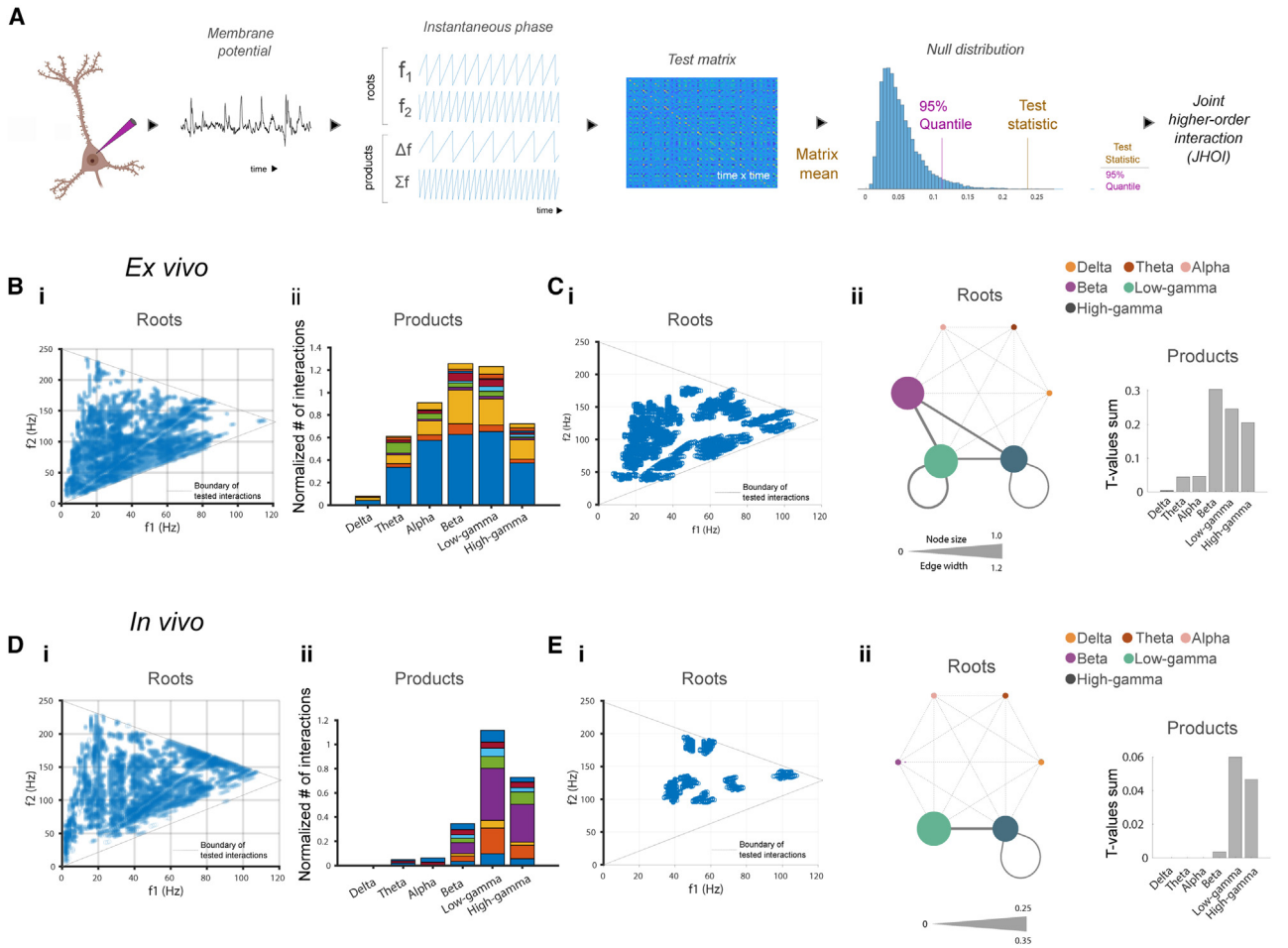

Figure 3. Endogenous membrane potential mixing in individual neurons *ex vivo* and *in vivo*

(A) Workflow to assess endogenous frequency mixing in cell membrane potential. For a given trace of endogenous membrane potential, the instantaneous phases of four frequency mixing components (roots: $f_1, f_2 > f_1$, products: $\Delta f = f_2 - f_1, \sum f = f_1 + f_2$) are extracted. Each subset of three phases (triplet) are used to construct a test matrix, which, when compared to a null distribution, defines the joint higher-order interaction (JHOI) strength heuristic.

(B and C) *Ex vivo* recordings.

(B) Frequency quadruplets with significant mixing in individual cells, assessed via permutation cluster test for each cell. Shown are (i) significant mixing root frequencies overlaid and (ii) the corresponding number of significant mixing interactions stacked by cell and normalized by the number of tested interactions per frequency band. $n = 20$ cells.

(C) Frequency quadruplets with significant mixing consistent across the cells, assessed via group-level permutation cluster test, showing (i) distribution of root frequencies overlaid and (ii) root frequencies stratified by frequency bands (network plot[†]) and distribution of frequency mixing products (bar chart). $n = 10$ cells.

(D and E) *In vivo* recordings.

(D) As in (B) but *in vivo*.

(E) As in (C) but *in vivo*. [†]Network plots: node size proportional to normalized sum of t-values of significant quadruplets within band (t test vs. surrogate); edge width as in node size for roots shared between bands.

stacked by cell and normalized by the number of tested interactions per frequency band. The mixing clusters within and between the beta and gamma bands were consistent across the cells (Figure 3C, computed via a permutation cluster test at the group level against surrogate data), suggesting that certain frequencies are more commonly mixed. Moreover, by taking the average mixing across all mixing interactions up to 250 Hz, we found significantly stronger mixing in the neural membrane potentials vs. surrogate data ($p = 0.0027$, paired t test, $n = 10$ cells). Adding a pharmacological blockade of the synaptic ion channel currents (as before) reduced the overall frequency mixing strength in the neural membrane potentials by approximately 30% (Figure S6A), particularly in a subset of high frequency mixing clusters (Figures S6B and S6C).

To explore whether endogenous membrane potential mixing also occurs in the intact rodent brain, we recorded the membrane potentials of individual neural cells *in vivo* using automated whole-cell patch clamp recordings[27] and deployed the same computation strategy to assess the phase dependency in all possible frequency mixing quadruplets. We found significantly

stronger frequency mixing in the spontaneous membrane potentials of the cells (mean JHOI amplitude across all mixing interactions up to 250 Hz: 0.596 ± 0.168, mean ± SD; n = 8 cells from 8 animals; p = 0.009; compared to surrogate). The membrane potentials of individual cells exhibited a variety of frequency mixing clusters, as in brain slices. The mixings produced a narrower range of frequencies in the beta and gamma bands (Figure 3D). Across the cells, the frequency mixing clusters were consistent in the gamma bands (Figure 3E), supporting an earlier report using LFP recording.[15]

Mixing of endogenous neural network oscillations in the human brain

After establishing the cellular origin of the neural frequency mixing phenomenon, we aimed to test whether the phenomenon exists in human brain oscillations, expanding on earlier evidence of mixing of endogenous neural network oscillations in rodents.[14,15] Neural oscillations are ubiquitous in the human brain.[28] We focused on the most salient human brain oscillation, i.e., the posterior alpha oscillation that can be readily observed in EEG during an awake, eyes-closed state,[29] and its established role in visual attention modulation.[30,31] We recorded awake, eyes-closed EEG in healthy human subjects (n = 20, mean age 29.3 ± 12.2 SD, 6 females) and subsequently measured their visual attention control using a feature-matching task.[32] We used the same computation strategy to examine the phase interaction in all possible frequency mixing quadruplets (up to 45 Hz) in EEG electrodes at a subset of sites in the parieto-occipital, temporal, and prefrontal regions (i.e., Pz, Oz, T7, T8, FP1, and FP2 of the international 10-10 system) implicated in visual attention control (Figure 4A).

We found a robust mixing of neural network oscillations between sites of the human brain (JHOI amplitude 0.4 ± 0.008, mean ± SD, p = 1.6e−16, paired t test vs. surrogate data). The spatial topology of the mixing is shown in Figure 4B, and the frequency band topology is shown in Figure 4C. The intersite mixings occurred between all brain regions and frequency bands (Figures S7A–S7C) yet were stronger between the delta and theta bands. We also found mixing within brain sites, i.e., between local oscillations (JHOI amplitude 0.4 ± 0.02, mean ± SD, p = 7.2e−12). The local mixings also occurred in all brain regions and frequency bands (Figures S7D–S7F), yet each brain region displayed a unique frequency band mixing pattern (Figures 4D–4F). The frontal region was dominated by theta-alpha mixing, while parieto-occipital was dominated by alpha mixing, and temporal regions by beta mixing. The strength of oscillation mixing was not correlated with the oscillation power (Figure S8A), implying that mixing is a distinct feature of brain oscillation dynamics.

As expected, a strong alpha oscillation dominated the participants' awake, eyes-closed EEG (Figure S8B). We found that the mixing strength of this alpha oscillation was correlated with the participants' visual attention capacity, indexed by the score in the subsequential feature-matching task (Figure 5A, R^2 = 0.363, p = 0.017, linear regression). A further investigation revealed that the alpha oscillation mixings associated with visual attention were specific to those with the beta oscillation (Figure 5B, R^2 = 0.497, p = 0.003, linear regression with Bonferroni correction for multiple comparisons). These alpha-beta mixings were strongest within the occipital cortex and between the occipital (alpha oscillation) and parietal (beta oscillation) cortices (Figure 5C, repeated-measures ANOVA F(2.48), p = 1.06e−5), producing new oscillations that were strongest in the gamma band (posteriorly) and weakest in the delta band (Figure 5D, repeated-measures ANOVA Oz-Oz F(2.6), p = 1.18e−5; Oz-Pz F(2.98), p = 8.5e−7). These results suggest that the visual attention capacity may be modulated by frequency mixing strength, i.e., the efficiency by which the salient posterior alpha oscillation is mixed to augment local synchronization in the gamma band.

DISCUSSION

The electrodynamics of the neural cell membrane underpins the brain's computational functions. Neurons sum minuscule electrochemical synaptic inputs across their dendritic trees to yield integrated transmembrane potentials that, above a threshold, evoke action potentials and subsequent electrochemical axonal outputs.[33–35] Nonlinear processes in the synapses and dendritic tree have been shown to enable complex signal processing[36–38], while subthreshold rhythms functionally coordinate the processing across distributed neurons.[20–23] In this paper, we report that the electrodynamics of the neural cell membrane involves mixing subthreshold rhythms, thereby actively producing new frequencies.

Our report expands on previous reports of frequency mixing in rodents[14,15] by demonstrating the single-cell origin of the phenomenon and its existence and functional relevance in humans. Our report strengthens hitherto evidence of single-cell multiplication based on the coincidence detection capacity (Gabbiani et al.,[10] Groschner et al.,[11] Lavzin et al.,[13] and Poleg-Polsky and Diamond[12]) by demonstrating the frequency mixing capacity. Our results suggest that the mixing of subthreshold frequencies occurs in the currents of the voltage-gated ion channels and that the mixing process is highly efficient. Specifically, the threshold for inducing spike trains by mixing frequencies in the normal neural range was similar to that by direct stimulation at the target frequency. The mixing efficiency of kHz electrical stimulation was 1.5–2 times weaker than with frequencies within the normal range. These results help elucidate the mechanism by which temporal interference of kHz electric fields stimulates neural activity.[18]

Earlier studies have shown evidence of a resonance phenomenon in individual neurons due to the low-pass filtering by the passive membrane conductance and the high-pass filtering by the active membrane conductance.[39] Could the observed generation of subthreshold rhythms have originated in a neural resonance rather than mixing? First, a resonance phenomenon predicts a large response to inputs near the resonant frequency and a smaller response at other frequencies.[40] In contrast, we found that the efficiency of generating subthreshold oscillations at the difference frequency was consistent across a wide range of average input frequencies spanning two orders of magnitude away from the prospective "resonance frequency." For example, the efficiency of generating a 10 Hz subthreshold oscillation with a average input frequency of 10 Hz was similar to generating it with a average input frequency of 1,000 Hz.

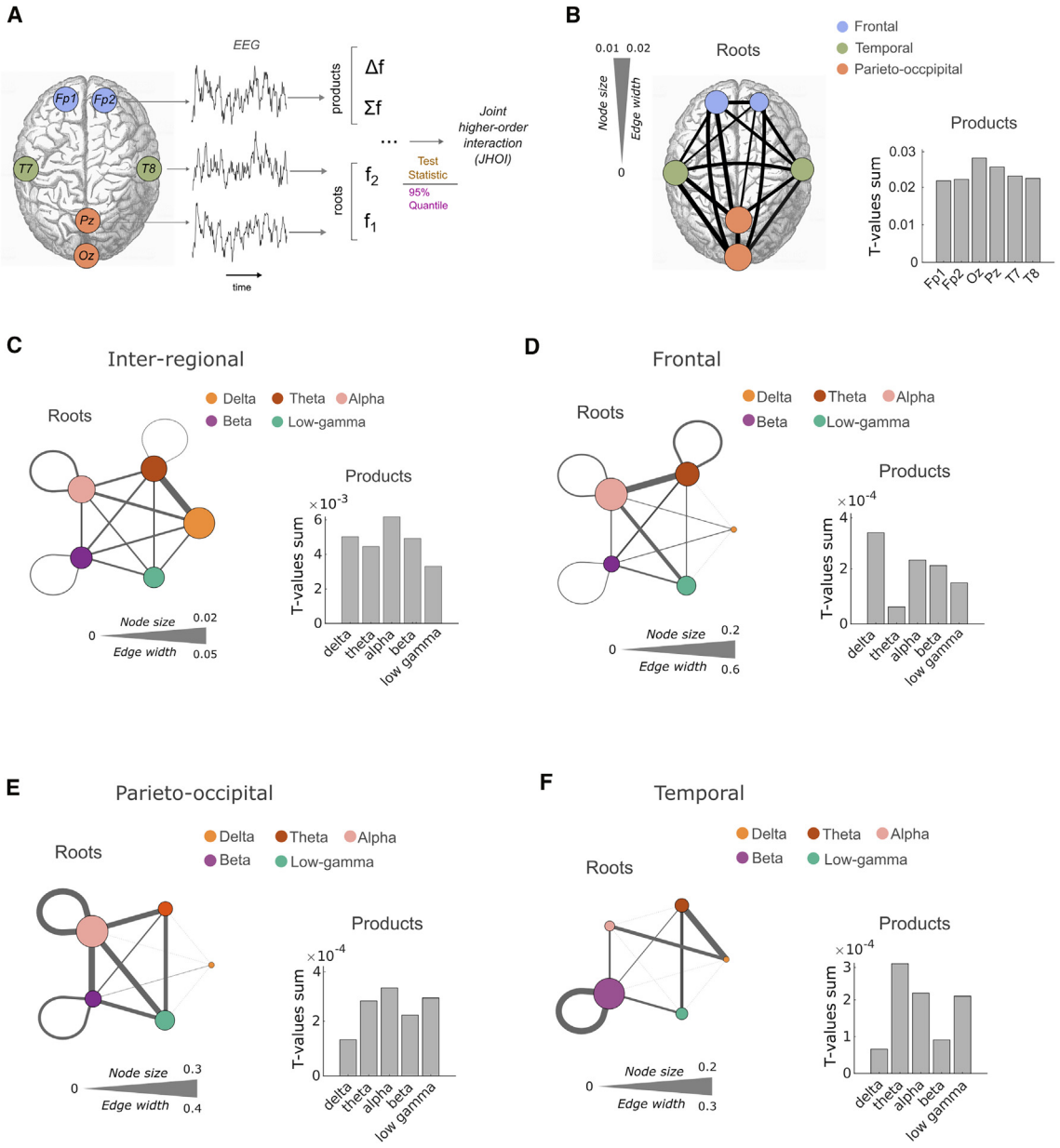

Figure 4. Mixing of endogenous neural network oscillations in the human brain EEG

(A) Illustration of workflow for assessing endogenous frequency mixing in the human brain EEG. Similar to Figure 3A but with instantaneous phases of the four frequency mixing components extracted from one or multiple cortical locations (in this example, roots: Pz and T8; products: Fp2).

(B and C) Mixing of neural network oscillations between cortical sites.

(B) Spatial topology of frequency mixing (significant at group-level against surrogate) for roots† (network plot) and products (bar chart).

(C) Bands topology of frequency mixing (significant at group-level against surrogate) for roots† (network plot) and products (bar chart).

(D–F) Mixing of neural network oscillations within cortical sites.

(D) Bands topology of frequency mixing (significant at group-level against surrogate) in the frontal brain region for roots† and products (network plot).

(E) As in (D) but in the parieto-occipital brain region.

(F) As in (D) but in the temporal brain region. †Network plots: node size proportional to normalized sum of t-values of significant quadruplets within band/channel (t test against surrogate); edge width is the same as node size but for roots shared between bands/channels. Boxplots: central line, median; circle, mean; whiskers, interquartile range; gray dots, outliers.

Second, a resonance phenomenon predicts an oscillation at a single frequency (i.e., the resonance frequency) and perhaps its harmonics.[39,41] In contrast, we found that when the average input frequency is sufficiently low (i.e., 7 + 17 Hz), the generated oscillations contained both the difference frequency (10 Hz) and the sum frequency (24 Hz), in agreement with a frequency mixing

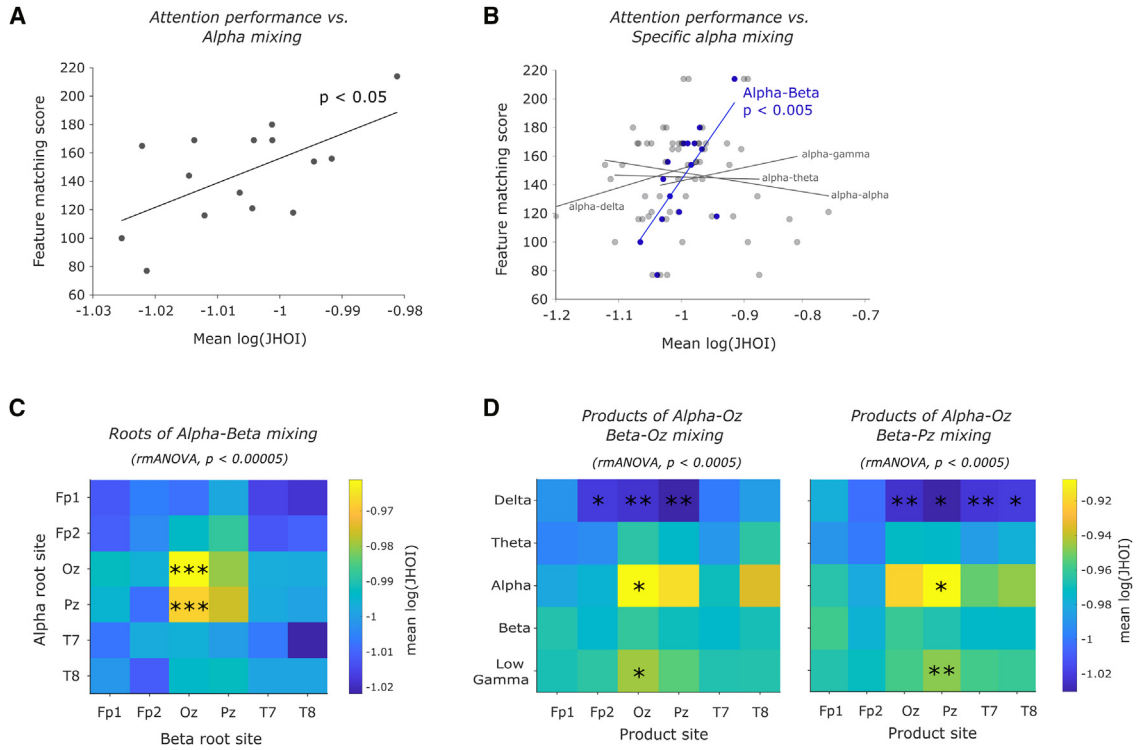

Figure 5. Human network oscillation mixing correlates with visual attention control

(A) Participants' feature-matching score vs. strength of all alpha oscillation mixings (log JHOI averaged across all intersite and local mixings), R^2 = 0.363, p = 0.017, linear regression.

(B) Participants' feature-matching score vs. strength of alpha oscillation mixing with specific bands, showing significance at alpha-beta mixing, R^2 = 0.497, p = 0.003, linear regression, Bonferroni corrected for multiple comparisons.

(C) Topology of attentional correlated alpha-beta mixing roots, showing strongest mixing within Oz and between Oz alpha and Pz beta. ***p < 0.001, post hoc paired t test comparisons.

(D) Topology of alpha-beta mixing products originated in Oz alpha-Oz beta (left) and Oz alpha-Pz beta (right), showing strongest products in posterior alpha and gamma bands and weakest products at delta band. *p < 0.05 and **p < 0.01; post hoc paired t test comparisons. rmANOVA, repeated measures ANOVA.

phenomenon but not a resonance phenomenon. Third, a resonance phenomenon predicts an oscillation at a specific frequency (i.e., the resonance frequency) independent of the input frequencies. In contrast, we found that the frequency of the subthreshold oscillations was dependent on the input frequencies. For example, when one input frequency was 4,997 Hz, the evoked oscillations were 5, 10, and 40 Hz, when the second input frequency was 5,002, 5,007, and 5,037 Hz, respectively, in agreement with a frequency mixing phenomenon but not a resonance phenomenon. Thus, the observed subthreshold rhythms originated in a mixing, not a resonance, cellular phenomenon.

Neural oscillations are ubiquitous in the human brain[28] and are implicated in regulating behavioral states,[42] coordinating multisensory processing,[43] and cognitive processes, such as memory and consciousness.[44] Aberrant oscillations have been associated with almost all neurological and psychiatric disorders.[45–48] The frequencies of neural oscillations have been thought to emerge from a competition between local oscillators since different oscillations can naturally emerge in neural networks with different cell-type compositions.[22] Our findings, together with the original studies in rodents,[14,15] suggest that individual neurons can control the frequencies of their network oscillations via a membrane-mixing phenomenon.

The brain has traditionally been modeled as a complex system composed of pairwise interactions among different elements. There is a growing acknowledgment that such a theory offers a limited description of brain function.[49,50] High-order interactions, which involve groups of three or more elements, are increasingly recognized as foundational to the architecture of many complex systems and appear to play a pivotal role in cognition.[51,52] Here, we posit that frequency mixing may be a fundamental mechanism for integrating high-order information across spatiotemporal scales. Our results suggest that the topology and strength of frequency mixing in the human brain have behavioral relevance. We show that the mixing of the salient posterior alpha-beta oscillations to produce gamma-band oscillations correlates with the visual attention state. There is substantial evidence that posterior alpha oscillation modulates visual cortex excitability and, consequentially, visual perception and attention (see, for example, Sadaghiani and Kleinschmidt[53]). The mixing of alpha and beta oscillations to produce gamma oscillations, which have been linked to spiking activity, may underpin the mechanism of excitability modulation. Our data show that each brain

region has a unique pattern of mixing oscillations modulated by inter-regional mixing, suggesting a mechanism coupling local and global oscillations (see also Doiron et al.'s[42] image-reject mixing in communication theory).

The functional role of neural oscillations has been linked to the coordination of spiking activity between brain sites because task-induced synchronization, i.e., phase alignment, aka functional connectivity, has been observed.[44] Our results imply that individual neurons could directly utilize these oscillations to perform advanced computational operations such as phase detection and (de)multiplexing that, until now, have only been seen in modern telecommunication.

Limitations of the study

In this study, we did not directly test the link between frequency mixing in the EEG oscillations and the frequency mixing in the subthreshold membrane potential of individual neurons. The fact that extracellular signals such as LFP and EEG oscillations originate predominantly from synchronous subthreshold activity of individual neurons[54] allows a conceptional link between the human EEG and single-neuron patch clamp results. However, future studies using concurrent single-cell and network-level recordings should further elucidate this link and could shed light on the precise mechanisms underpinning the integration of high-order computations across different scales. Further studies are also needed to pinpoint the contribution of different ion channels not tested here and passive membrane properties to the frequency mixing phenomenon.

STAR★METHODS

Detailed methods are provided in the online version of this paper and include the following:

- KEY RESOURCES TABLE
- RESOURCE AVAILABILITY
  - Lead contact
  - Materials availability
  - Data and code availability
- EXPERIMENTAL MODEL AND STUDY PARTICIPANT DETAILS
  - Single-cell investigation *ex vivo*
  - Single-cell investigation *in vivo*
  - Human investigation
- METHOD DETAILS
  - Single-cell investigation *ex vivo*
  - Single-cell investigation *in vivo*
  - Human investigation
- QUANTIFICATION AND STATISTICAL ANALYSIS
  - Single-cell investigation *ex vivo*: Exogenous frequency mixing
  - Single-cell investigation *in vivo*/human investigation: endogenous frequency mixing
  - Statistical analysis

SUPPLEMENTAL INFORMATION

Supplemental information can be found online at https://doi.org/10.1016/j.celrep.2024.114274.

ACKNOWLEDGMENTS

We thank Lok Fan for improving computational efficiency, Yuval Gal Shohet for discussions on JHOI measure, Matteo Vinao-Carl for providing input on the discussion, Dr. Ho-Jun Suk for assisting with *in vivo* patch clamp experiments, and Dr. Carola Radulescu and Dr. Sam Barnes for help in setting up the *ex vivo* patch clamp experimental rig. This work was funded by Deutsche Forschungsgemeinschaft, DFG, German Research Foundation, Project-ID 424778381-TRR 295 (R.P.); EPSRC award EP/N014529/1 supporting the EPSRC Center for Mathematics of Precision Healthcare at Imperial College London (R.P., F.L., M.B.); the UK Dementia Research Institute—an initiative funded by the Medical Research Council (N.G., C.E.L.); the Engineering and Physical Sciences Research Council, UK, EP/W004844/1 (N.G.); and the National Institute for Health and Care Research, Imperial Biomedical Research Center (N.G.). Schematic subfigures created with BioRender.com.

AUTHOR CONTRIBUTIONS

Conceptualization, N.G., C.E.L., and R.P.; methodology, C.E.L., R.P., and F.L.; investigation, C.E.L., R.P., and E.-J.M.; visualization, C.E.L., R.P., and E.R.; supervision, N.G., M.B., E.S.B., and D.J.S.; writing, N.G., C.E.L., R.P., E.R., and E.-J.M.

DECLARATION OF INTERESTS

N.G. and E.S.B. are inventors of a patent on neuromodulation using temporal interference (TI) of kHz electric fields, assigned to MIT. N.G. and E.S.B. are co-founders of TI Solutions AG, a company committed to producing hardware and software solutions to support TI research.

Received: March 8, 2023
Revised: December 18, 2023
Accepted: May 9, 2024
Published: May 25, 2024

REFERENCES

1. Goldsmith, A. (2005). Wireless communications. Wirel. Commun, 1–644. https://doi.org/10.1017/CBO9780511841224.
2. Protopopov, V.V. (2009). Principles of optical heterodyning. Springer Ser. Opt. Sci. *149*, 1–49. https://doi.org/10.1007/978-3-642-02338-5_1.
3. Srinivasan, M.V., and Bernard, G.D. (1976). A proposed mechanism for multiplication of neural signals. Biol. Cybern. *21*, 227–236. https://doi.org/10.1007/BF00344168.
4. Andersen, R.A., Essick, G.K., and Siegel, R.M. (1985). Encoding of spatial location by posterior parietal neurons. Science *230*, 456–458. https://doi.org/10.1126/science.4048942.
5. Peña, J.L., and Konishi, M. (2001). Auditory spatial receptive fields created by multiplication. Science *292*, 249–252. https://doi.org/10.1126/science.1059201.
6. Huston, S.J., and Krapp, H.G. (2009). Nonlinear integration of visual and haltere inputs in fly neck motor neurons. J. Neurosci. *29*, 13097–13105. https://doi.org/10.1523/JNEUROSCI.2915-09.2009.
7. Haag, J., Wertz, A., and Borst, A. (2010). Central gating of fly optomotor response. Proc. Natl. Acad. Sci. USA *107*, 20104–20109. https://doi.org/10.1073/pnas.1009381107.
8. Hatsopoulos, N., Gabbiani, F., and Laurent, G. (1995). Elementary computation of object approach by a wide-field visual neuron. Science *270*, 1000–1003. https://doi.org/10.1126/science.270.5238.1000.
9. Hassenstein, B., and Reichardt, W. (1956). Systemtheoretische Analyse der Zeit-Reihenfolgen-und Vorzeichenauswertung bei der Bewegungsperzeption des Rüsselkäfers Chlorophanus. Z. Naturforschung - Sect. B J. Chem. Sci. *11*, 513–524. https://doi.org/10.1515/znb-1956-9-1004.
10. Gabbiani, F., Krapp, H.G., Koch, C., and Laurent, G. (2002). Multiplicative computation in a visual neuron sensitive to looming. Nature *420*, 320–324. https://doi.org/10.1038/nature01190.
11. Groschner, L.N., Malis, J.G., Zuidinga, B., and Borst, A. (2022). A biophysical account of multiplication by a single neuron. Nature *603*, 119–123. https://doi.org/10.1038/s41586-022-04428-3.

12. Poleg-Polsky, A., and Diamond, J.S. (2016). NMDA Receptors Multiplicatively Scale Visual Signals and Enhance Directional Motion Discrimination in Retinal Ganglion Cells. Neuron *89*, 1277–1290. https://doi.org/10.1016/j.neuron.2016.02.013.

13. Lavzin, M., Rapoport, S., Polsky, A., Garion, L., and Schiller, J. (2012). Nonlinear dendritic processing determines angular tuning of barrel cortex neurons in vivo. Nature *490*, 397–401. https://doi.org/10.1038/nature11451.

14. Ahrens, K.F., Levine, H., Suhl, H., and Kleinfeld, D. (2002). Spectral mixing of rhythmic neuronal signals in sensory cortex. Proc. Natl. Acad. Sci. USA *99*, 15176–15181. https://doi.org/10.1073/pnas.222547199.

15. Haufler, D., and Paré, D. (2019). Detection of Multiway Gamma Coordination Reveals How Frequency Mixing Shapes Neural Dynamics. Neuron. https://doi.org/10.1016/j.neuron.2018.12.028.

16. Kleinfeld, D., and Mehta, S.B. (2006). Spectral Mixing in Nervous Systems: Experimental Evidence and Biologically Plausible Circuits. Prog. Theor. Phys. Suppl. *161*, 86–98. https://doi.org/10.1143/PTPS.161.86.

17. Violante, I.R., Alania, K., Cassarà, A.M., Neufeld, E., Acerbo, E., Carron, R., Williamson, A., Kurtin, D.L., Rhodes, E., Hampshire, A., et al. (2023). Non-invasive temporal interference electrical stimulation of the human hippocampus. Nat. Neurosci. *26*, 1994–2004. https://doi.org/10.1038/s41593-023-01456-8.

18. Grossman, N., Bono, D., Dedic, N., Kodandaramaiah, S.B., Rudenko, A., Suk, H.-J., Cassara, A.M., Neufeld, E., Kuster, N., Tsai, L.-H., et al. (2017). Noninvasive Deep Brain Stimulation via Temporally Interfering Electric Fields. Cell *169*, 1029–1041.e16.

19. Kasten, F.H., Negahbani, E., Fröhlich, F., and Herrmann, C.S. (2018). Non-linear transfer characteristics of stimulation and recording hardware account for spurious low-frequency artifacts during amplitude modulated transcranial alternating current stimulation (AM-tACS). Neuroimage *179*, 134–143. https://doi.org/10.1016/j.neuroimage.2018.05.068.

20. Hutcheon, B., Miura, R.M., and Puil, E. (1996). Subthreshold membrane resonance in neocortical neurons. J. Neurophysiol. *76*, 683–697. https://doi.org/10.1152/jn.1996.76.2.683.

21. Richardson, M.J.E., Brunel, N., and Hakim, V. (2003). From subthreshold to firing-rate resonance. J. Neurophysiol. *89*, 2538–2554. https://doi.org/10.1152/jn.00955.2002.

22. Buzsáki, G., and Draguhn, A. (2004). Neuronal oscillations in cortical networks. Science *304*, 1926-9. https://doi.org/10.1126/science.1099745.

23. Giocomo, L.M., Zilli, E.A., Fransén, E., and Hasselmo, M.E. (2007). Temporal frequency of subthreshold oscillations scales with entorhinal grid cell field spacing. Science *315*, 1719-22. https://doi.org/10.1126/science.1139207.

24. Lancaster, H.O. (2004). Chi-Square Distribution. In Encyclopedia of Statistical Sciences. https://doi.org/10.1002/0471667196.ess0238.

25. Rubenstein, P.K., Chwialkowski, K.P., and Gretton, A. (2016). A kernel test for three-variable interactions with random processes. In 32nd Conference on Uncertainty in Artificial Intelligence 2016, UAI 2016.

26. Sejdinovic, D., Gretton, A., and Bergsma, W. (2013). A kernel test for three-variable interactions. In Advances in Neural Information Processing Systems.

27. Kodandaramaiah, S.B., Franzesi, G.T., Chow, B.Y., Boyden, E.S., and Forest, C.R. (2012). Automated whole-cell patch-clamp electrophysiology of neurons in vivo. Nat. Methods *9*, 585–587. https://doi.org/10.1038/nmeth.1993.

28. Buzsáki, G., Logothetis, N., and Singer, W. (2013). Scaling brain size, keeping timing: Evolutionary preservation of brain rhythms. Neuron *80*, 751–764. https://doi.org/10.1016/j.neuron.2013.10.002.

29. Berger, H. (1929). Über das Elektrenkephalogramm des Menschen (Arch. Für Psychiatr. Nervenkrankh). https://doi.org/10.1007/BF01797193.

30. Fries, P., Reynolds, J.H., Rorie, A.E., and Desimone, R. (2001). Modulation of oscillatory neuronal synchronization by selective visual attention. Science *291*, 1560–1563. https://doi.org/10.1126/science.1055465.

31. Carrasco, M. (2011). Visual attention: The past 25 years. Vision Res *51*, 1484–1525. https://doi.org/10.1016/j.visres.2011.04.012.

32. Hampshire, A., Highfield, R.R., Parkin, B.L., and Owen, A.M. (2012). Fractionating Human Intelligence. Neuron *76*, 1225–1237. https://doi.org/10.1016/j.neuron.2012.06.022.

33. Bean, B.P. (2007). The action potential in mammalian central neurons. Nat. Rev. Neurosci. *8*, 451–465. https://doi.org/10.1038/nrn2148.

34. Colbert, C.M., and Pan, E. (2002). Ion channel properties underlying axonal action potential initiation in pyramidal neurons. Nat. Neurosci. *5*, 533–538. https://doi.org/10.1038/nn0602-857.

35. Aidley, D.J. (1978). The physiology of excitable cells. https://doi.org/10.1093/ptj/52.5.599.

36. Silver, R.A. (2010). Neuronal arithmetic. Nat. Rev. Neurosci. *11*, 474–489. https://doi.org/10.1038/nrn2864.

37. Koch, C., and Segev, I. (2000). The role of single neurons in information processing. Nat. Neurosci. *10*, 1038–81444.

38. Beniaguev, D., Segev, I., and London, M. (2021). Single cortical neurons as deep artificial neural networks. Neuron *109*, 2727–2739.e3. https://doi.org/10.1016/j.neuron.2021.07.002.

39. Hutcheon, B., and Yarom, Y. (2000). Resonance, oscillation and the intrinsic frequency preferences of neurons. Trends Neurosci. *23*, 216–222. https://doi.org/10.1016/S0166-2236(00)01547-2.

40. Weik, M.H. (2001). heterodyning. In Computer Science and Communications Dictionary, M.H. Weik, ed. (Springer US), p. 720. https://doi.org/10.1007/1-4020-0613-6_8322.

41. Petosa, A. (2007). Dielectric Resonator Antenna Handbook (Artech).

42. Doiron, B., Litwin-Kumar, A., Rosenbaum, R., Ocker, G.K., and Josić, K. (2016). The mechanics of state-dependent neural correlations. Nat. Neurosci. *19*. https://doi.org/10.1038/nn.4242.

43. Keil, J., and Senkowski, D. (2018). Neural Oscillations Orchestrate Multisensory Processing. Neuroscientist *24*, 609–626. https://doi.org/10.1177/1073858418755352.

44. Ward, L.M. (2003). Synchronous neural oscillations and cognitive processes. Trends Cogn Sci *7*, 553–559. https://doi.org/10.1016/j.tics.2003.10.012.

45. Uhlhaas, P.J., and Singer, W. (2006). Neural Synchrony in Brain Disorders: Relevance for Cognitive Dysfunctions and Pathophysiology. Neuron *52*, 155–168. https://doi.org/10.1016/j.neuron.2006.09.020.

46. Nimmrich, V., Draguhn, A., and Axmacher, N. (2015). Neuronal Network Oscillations in Neurodegenerative Diseases. NeuroMolecular Med. *17*, 270–284. https://doi.org/10.1007/s12017-015-8355-9.

47. Başar, E. (2013). Brain oscillations in neuropsychiatric disease. Dialogues Clin. Neurosci. https://doi.org/10.31887/dcns.2013.15.3/ebasar.

48. Vanneste, S., Song, J.J., and De Ridder, D. (2018). Thalamocortical dysrhythmia detected by machine learning. Nat. Commun. *9*, 1103. https://doi.org/10.1038/s41467-018-02820-0.

49. Battiston, F., Amico, E., Barrat, A., Bianconi, G., Ferraz de Arruda, G., Franceschiello, B., Iacopini, I., Kéfi, S., Latora, V., Moreno, Y., et al. (2021). The physics of higher-order interactions in complex systems. Nat. Phys. *17*, 1093–1098. https://doi.org/10.1038/s41567-021-01371-4.

50. Lambiotte, R., Rosvall, M., and Scholtes, I. (2019). From networks to optimal higher-order models of complex systems. Nat. Phys. *15*, 313–320. https://doi.org/10.1038/s41567-019-0459-y.

51. Gatica, M., Cofré, R., Mediano, P.A.M., Rosas, F.E., Orio, P., Diez, I., Swinnen, S.P., and Cortes, J.M. (2021). High-Order Interdependencies in the Aging Brain. Brain Connect. *11*, 734–744. https://doi.org/10.1089/brain.2020.0982.

52. Tononi, G., Boly, M., Massimini, M., and Koch, C. (2016). Integrated information theory: from consciousness to its physical substrate. Nat. Rev. Neurosci. *17*, 450–461. https://doi.org/10.1038/nrn.2016.44.

53. Sadaghiani, S., and Kleinschmidt, A. (2016). Brain Networks and α-Oscillations: Structural and Functional Foundations of Cognitive Control. Trends Cogn Sci *20*. https://doi.org/10.1016/j.tics.2016.09.004.

54. Buzsáki, G., Anastassiou, C.A., and Koch, C. (2012). The origin of extracellular fields and currents-EEG, ECoG, LFP and spikes. Nat. Rev. Neurosci. *13*, 407–420. https://doi.org/10.1038/nrn3241.

55. Deans, J.K., Powell, A.D., and Jefferys, J.G.R. (2007). Sensitivity of coherent oscillations in rat hippocampus to AC electric fields. J. Physiol. *583*, 555–565. https://doi.org/10.1113/jphysiol.2007.137711.

56. Berlinet, A., and Thomas-Agnan, C. (2004). Reproducing Kernel Hilbert Spaces in Probability and Statistics. https://doi.org/10.1007/978-1-4419-9096-9.

57. Mammen, E. (1993). Bootstrap and Wild Bootstrap for High Dimensional Linear Models. Ann. Stat. *21*. https://doi.org/10.1214/aos/1176349025.

58. Schreiber, T., and Schmitz, A. (2000). Surrogate time series. Phys. Nonlinear Phenom. *142*, 346–382. https://doi.org/10.1016/S0167-2789(00)00043-9.

STAR★METHODS

KEY RESOURCES TABLE

REAGENT or RESOURCE	SOURCE	IDENTIFIER
Chemicals, peptides, and recombinant proteins		
NBQX	Merck Life Sciences, UK	#N183
DAP-5	Merck Life Sciences, UK	#A8054
Bicuculline	Merck Life Sciences, UK	#14340
TTX	Abcam, UK	#ab120054
Deposited data		
Patch clamp data, Zenodo (repository)	This study	https://doi.org/10.5281/zenodo.10992758
Experimental models: Organisms/strains		
Mouse: C57BL/6J	Charles River, UK/The Jackson Laboratory, USA	Strain: #027/#000664
Software and algorithms		
JHOI frequency mixing toolbox (freqmix), Zenodo (repository)	This study	https://doi.org/10.5281/zenodo.10992758
JHOI frequency mixing toolbox (freqmix), GitHub (repository)	This study	https://github.com/ImperialCollegeLondon/freqmix
Other		
Voltage waveform generator	National Instruments, UK	Model: USB-6216 BNC
Constant current source	Soterix Medical Inc, NY, USA	Model: LCI1107
Platinum wire	VWR, UK	Cat: 45093.BU

RESOURCE AVAILABILITY

Lead contact

Further information and requests for resources and reagents should be directed to and will be fulfilled by the lead contact, Nir Grossman (nirg@imperial.ac.uk).

Materials availability

This study did not generate unique reagents.

Data and code availability

All mouse patch clamp data have been deposited at Zenodo and are publicly available as of the date of publication. The DOI is listed in the Key resources table. The participants of this study did not give written consent for their data to be shared publicly, so raw EEG data is not available.

All original code used in this study has been deposited at Zenodo, while updated versions of the JHOI frequency mixing software are available at GitHub. Both are publicly available as of the date of publication. The DOI is listed in the Key resources table.

Any additional information required to reanalyze the data reported in this paper is available from the lead contact upon request.

EXPERIMENTAL MODEL AND STUDY PARTICIPANT DETAILS

Single-cell investigation *ex vivo*

Animals

All mice were male C57BL/6, aged between 4 and 12 weeks. Mice were housed in standard cages in the Imperial College London animal facility, with *ad libitum* food and water in a controlled light-dark cycle environment, with standard monitoring by veterinary staff. The Imperial College London's Animal Welfare and Ethical Review Board approved all animal procedures, and all experiments were performed in accordance with relevant regulations/according to the United Kingdom Animals (Scientific Procedures) Act 1986.

Single-cell investigation *in vivo*

Animals

All mice were male C57BL/6, aged between 4 and 12 weeks. Mice were housed in standard cages in the Massachusetts Institute of Technology (MIT) animal facility, with *ad libitum* food and water in a controlled light-dark cycle environment, with standard monitoring by veterinary staff. All animal procedures were approved by the MIT Committee on Animal Care (CAC, Protocol Number: 1115-111-18), and all experiments conformed to the relevant regulatory standards.

Human investigation

Participants

Twenty healthy adults (14 males, 6 females; mean age 29.29, range 18–70 years) were included. Written informed consent was obtained for all participants judged to have capacity according to the declaration of Helsinki. Human data was collected under approval by the West London Research Ethics Committee (09/HO707/82).

METHOD DETAILS

Single-cell investigation *ex vivo*

Brain slice preparation

Anesthesia of mice was achieved via intraperitoneal injection of 100 mg/kg ketamine and 10 mg/kg xylazine. Mice were transcardially perfused with 0–5°C carbogenated dissection artificial cerebrospinal fluid (aCSF) containing (in mM): 108 $C_5H_{14}ClNO$, 3 KCl, 26 $NaHCO_3$, 1.25 NaH_2PO_4, 25 Dextrose, 3 C_3H_3NaO, 1 $MgCl_2$, and 2 $CaCl_2$. 350-μm-thick coronal slices around the somatosensory cortex were prepared using a Vibratome (Campden Instruments LTD, Loughborough, UK). Following sectioning, slices recovered for 2–4 h at room temperature in carbogenated bath aCSF containing (in mM): 120 NaCl, 3 KCl, 23 $NaHCO_3$, 1.25 NaH_2PO_4, 1 $MgCl_2$, and 2 $CaCl_2$. Following recovery, slices were placed in the recording chamber of an upright microscope (Scientifica, Uckfield, UK), and held down using a harp (Multi Channel Systems, Reutlingen, Germany). The recording chamber was continually perfused with room temperature carbogenated bath aCSF throughout the experiment.

Whole-cell patch clamp recording

Patch electrodes were pulled from filamented thin-walled borosilicate glass capillaries (World Precision Instruments, Hitchin, UK) using a horizontal Flaming–Brown micropipette puller (P1000; Sutter Instruments, Novato, CA, USA). Electrode tip resistance immediately after pulling ranged from 5 to 8 MΩ. Whole cell recordings were taken in a current clamp mode (no holding current) using a patch clamp amplifier (MultiClamp 700B; Molecular Devices Ltd). The recorded traces were digitalized using a digitiser (Digidata 1550b; Molecular Devices Ltd) at 100 kS/s rate. Recordings were obtained from the soma of L2/3 cortical neurons in coronal brain slices. Patch electrodes were filled with internal solution containing (in mM): 130 $KMeSO_4$, 8 NaCl, 2 KH_2PO_4,2 Dextrose and 10 HEPES. Following successful break-in and before each electrical stimulation, a protocol comprising of current steps increasing in amplitude by 50pA was run, to determine viability of the cell, resting membrane potential, and threshold for AP firing.

Electrical stimulation

Stimulating current waveforms were generated using a custom-written MATLAB GUI via an arbitrary voltage waveform generator (USB-6216 BNC; National Instruments, Newbury, UK) sampled at 250 kS/s and an isolated constant current source (LCI1107; Soterix Medical Inc, New York, NY, USA). The current waveforms were applied to the tissue via a 0.25mm diameter platinum wire electrode (VWR, Lutterworth, UK) positioned 50-100μm from the recorded neuron, touching the slice, on L2/3 cortex. The stimulating electrode was paired with two remote 2 × 2mm Ag/AgCl electrodes (VWR, Lutterworth, UK) in a y-shape configuration. The stimulation protocol included a series of two symmetrical biphasic sinusoidal waveforms with the same amplitude and a difference frequency (typically 10 Hz). The two sinusoidal waveforms were summed before they were applied to the tissue resulting in a combined waveform that oscillates at the average frequency and has an envelope amplitude that changes periodically at the difference frequency. We tested stimulation conditions with an average frequency between ∼10 Hz and ∼5,000 Hz and a range of current amplitudes (0.5mA current steps). Each stimulation condition was applied for 5s with 0.5s ramp-up, 0.5s ramp-down, and a 5s stimulation-free period between consecutive stimulations (baseline). The order of the stimulation conditions was randomized between recordings. Current density at the electrodes was estimated by dividing the applied current amplitude by the cross-sectional area of the stimulation electrodes.

Pharmacological manipulation

Blockade of synaptic ligand-gated ion channels was achieved by application of an AMPA receptor antagonist (NBQX; Merck Life Sciences Ltd, UK, #N183), an NMDA receptor antagonist (DAP-5; Merck Life Sciences, Ltd, UK, #A8054) and GABAA antagonist (Bicuculline; Merck Life Sciences Ltd, UK, #14340) to the bath aCSF being perfused to the slice. The resulting bath aCSF solution contained (in μM): 10 NBQX, 50 DAP-5, and 10 Bicuculline. One minute of spontaneous membrane potential activity was recorded prior to drug application and 10 min following, to observe elimination of postsynaptic potentials. Elimination of postsynaptic potentials was observed in 100% of cells included in analysis. Blockade of voltage-gated sodium channels was achieved by application of Tetrodotoxin (TTX) (Abcam Ltd, UK, #ab120054) to the bath aCSF being perfused to the slice. The resulting aCSF solution contained in μM): 1 TTX. Membrane potential response to current steps of 50pA was recorded prior to drug application and 10 min following, to observe elimination of action potentials (APs). Disappearance of APs was observed in 100% of cells included in analysis. Post drug stimulation and recordings commenced 10 min following drug application in all cases.

Single-cell investigation *in vivo*

Surgery

On the day of the experiment, the mice were injected with Meloxicam (1 mg/kg) and buprenorphine (0.1 mg/kg) and anesthetized with 1%–2% (v/v) isoflurane in oxygen. Ophthalmic ointment (Puralube Vet Ointment, Dechra, KS; USA) was applied to the eyes. The scalp and was shaved and sterilized with Betadine and 70% ethanol, a custom-made head-plate was attached using dental cement (C&B Metabond, Parkell, NY; USA), and a craniotomy was performed.

Whole-cell patch clamp recording

In vivo whole cell patching in current clamp mode was conducted in the cortex (depth of ~500 μm below the dura) of anesthetized mice with an autopatcher.[27] Whole cell recordings were taken in a current clamp mode (no holding current) using a patch clamp amplifier (MultiClamp 700B; Molecular Devices Ltd, Wokingham, UK). The recorded traces were digitalized using a digitiser (Digidata 1550b; Molecular Devices Ltd, Wokingham, UK) at 25 kS/s rate. Patch electrodes were pulled from thin-walled borosilicate glass capillary tubing using a pipette puller (P97; Sutter Instruments, Novato, CA, USA). Tip electrode resistance was 4.6–7.4 MΩ in artificial cerebrospinal fluid (ACSF), containing (in mM): 126 NaCl, 3 KCl, 1.25 NaH_2PO_4, 2 $CaCl_2$, 2 $MgSO_4$, 24 $NaHCO_3$ and 10 glucose. The patch electrode internal solution consisted of (in mM) 122.5 potassium gluconate, 12.5 KCl, 10 KOH-HEPES, 0.2 KOH-EGTA, 2 Mg-ATP, 0.3 Na_3-GTP, 8 NaCl (pH 7.35, mOsm 296. Following successful break-in and before each electrical stimulation, a membrane test was run on the cell to gather membrane statistics. Furthermore, a protocol comprising of current steps increasing in amplitude by 50pA was run, to determine viability of the cell.

Human investigation

EEG recording

A 32-channel active electrode standard actiCAP (Easycap) was used to acquire 5 min of eyes-closed resting state EEG data. Measurements were taken from nasion to inion and from left to right tragus to position the cap in accordance with the international 10–20 system with the vertex electrode (Cz) in the center. The cap was secured with a chin strap to maintain positioning. A small amount of conductive electrode gel was applied to each electrode using a blunt needle. Impedances for ground (Fpz) and reference (Fz) electrodes were maintained at <5kΩ and aimed to be kept under 50kΩ across all other electrodes. Signals from the electrodes were amplified using the actiCHamp system and data were recorded using the BrainVision Recorder software (Brain Products GmbH, Gilching, Germany) at a sampling rate of 1 kHz. Six channels were exported for further analysis as representative of the frontal (Fp1, Fp2), temporal (T7, T8) and parieto-occipital (Pz, Oz) regions. One minute of artifact-free resting-state EEG for each subject was then analyzed using the methodology introduced below. For spectral analysis, the traditional EEG bands were defined as follows: delta (0-4 Hz), theta (4-8 Hz), alpha (8-13 Hz), beta (13-30 Hz) and low-gamma (30-45 Hz).

Visual attentional control task

Visual attentional control was assessed using a feature-matching task delivered on a touchscreen tablet device using a custom-programmed application. The task included two grids presented side by side each containing a series of shapes. The shapes presented in each grid were identical for half of all trials and differed by one shape in the other half of trials. The participant was requested to state whether the shapes match or mismatch. The first trial contained one shape in each grid. The number of shapes increased with each correct response and decreased with each incorrect response. The task lasted for 90 s during which the participants solved as many trials as possible. The main outcome measure was the total score. Population mean = 131.35, SD = 32.79.[32]

QUANTIFICATION AND STATISTICAL ANALYSIS

All data were analyzed in MATLAB (MATLAB 2019a, The MathWorks Inc.).

Single-cell investigation *ex vivo*: Exogenous frequency mixing

Characterization of measurement's intermodulation distortions (IMDs)

Nonlinearity in the stimulation hardware can result in frequency mixing that can confound the measured neural signals at the frequency mixing products (i.e., Δf, $\sum f$, $2f_1$, $2f_2$, $2\Delta f$, etc.), aka intermodulation distortions (IMDs). Additional IMDs can arise from the recording hardware due to the large stimulation voltage at the amplifier input that risks shifting the dynamic range to a nonlinear gain. In our case, IMDs from the recording hardware were neglected as the amplifier operated in its linear gain range (tested by applying amplitude-modulated waveforms at different voltages directly to the amplifier). Whereas a high-pass filter could mitigate artifacts in the difference frequencies at the output of the current sources, artifacts in the sum frequencies were more challenging to mitigate in our experiment due to the spectral proximity to the applied frequencies and the smaller signal-to-noise-ratio (the amplitude of the transmembrane potential drops with frequency[55]). We characterized the measurement IMDs by repeating the experiments without brain slices and computing the root mean square (RMS) amplitude of the frequency mixing product of interest as in 'Subthreshold depolarization analysis' (see below). The artifactual stimulation potentials recorded at the applied frequencies (f_1, f_2) were amplitude matched and had the same stimulation artifact amplitude as those measured in the *ex vivo* condition ($p > 0.05$, Wilcoxon rank-sum test or two-sample t test).

Subthreshold depolarization analysis

Induced subthreshold membrane oscillation amplitude at the frequency mixing products (i.e., Δf, $\sum f$, $2f_1$, $2f_2$, $2\Delta f$, $2f_1$-f_2, $\sum f$- $2\Delta f$) was computed. The membrane potential trace in response to the maximum stimulation amplitude that had no APs was taken. The signals were filtered using a high-pass filter (Butterworth; 1 Hz, order 3) and a low-pass filter (Butterworth; 50 Hz, order 5) to remove DC shift and stimulation artifact. Traces were then bandpass filtered around the frequency of interest (±1 Hz) (Butterworth; bandwidth 2 Hz, order: 5). The average stimulation-induced subthreshold oscillation amplitude for each neuron was computed by computing RMS of the middle 1s of the filtered signal. For all analysis of subthreshold neural activity in the frequency and time domains, only recordings during stimulation where the neuron did not exhibit a suprathreshold response were included, to ensure that the values being obtained were representative of purely subthreshold neural polarization for that neuron. The RMS amplitudes at the frequencies of interest were tested against artifactual amplitude from the measurement's IMDs, and baseline amplitude at those frequencies (i.e., prior to the stimulation onset). Specifically, the baseline RMS amplitude was subtracted from the stimulation RMS amplitude and then statistically compared to the computed IMD RMS amplitude (also baseline subtracted) using the Wilcoxon rank-sum test or two-sample t test. See 'Characterization of measurement's intermodulation distortions (IMDs)' for details about the IMD measurement.

Threshold of inducing action potential (AP) train at Δf

To remove the stimulation voltage artifact at the applied frequencies, the traces were low pass filtered if the applied mean frequency was $\geq$ 100 Hz (Butterworth: cut-off frequency: 25 Hz; order: 5), or high pass filtered if $<$ 100 Hz (Butterworth: cut-off frequency: 100 Hz; order: 3). Threshold was defined as the lowest applied current density required to evoke an action potential (AP) train with at least three spikes significantly phase locked to the stimulation (tested using the Rayleigh test). APs were detected via a custom-made script using a peak finding algorithm. Thresholds were normalized to the threshold for direct stimulation with the difference frequency (10 Hz) for each neuron.

Plotted traces

For plotting of mean membrane potential, individual membrane potential traces were high-pass filtered to remove offset (Butterworth: cut-off frequency: 1 Hz; order: 3), and low pass filtered to remove stimulation artifact (Butterworth: cut-off frequency: 25 Hz; order: 5). The baseline membrane potential prior to each stimulation was computed as the mean membrane potential during the 0.5s preceding the stimulation (i.e., during the inter-stimulation interval).

Single-cell investigation *in vivo*/human investigation: endogenous frequency mixing

All data were analyzed in MATLAB (MATLAB 2021a, The MathWorks Inc.).

Overview

Frequency mixing, at the most basic level, involves the non-linear interaction of two root frequencies generating two product frequencies (the sum and difference of the root frequencies). The four frequencies form a frequency mixing quadruplet and any subset of three frequencies within the quadruplet form a frequency mixing triplet. The frequency mixing triplets display a 3-way phase relationship between the frequencies within the triplet, where there exist no underlying pairwise phase relationships,[15] i.e., the joint distribution of three instantaneous phase signals cannot be factorised. However, given that a 3-way phase relationship can exist, a 4-way phase relationship cannot be directly detected since it would be confounded by any potential underlying 3-way phase relationships (the joint distribution of four instantaneous phase signals can be factorised). Thus, to detect frequency mixing, we (1) detected frequency mixing triplets using the Lancaster interaction measure and Wild Bootstrap, (2) computed a heuristic measure of joint higher order interaction (JHOI) and (3) inferred the presence of frequency mixing quadruplets using the 4 subset triplets that constitute a quadruplet. Note, quadruplets, but not triplets alone, can reveal the underlying root frequencies.

Procedure

We computed the test statistic of the joint interaction for each frequency triplet by first computing the Gram matrices of the three instantaneous phase traces (computed via a Morlet wavelet decomposition with a width of 15 as in[15]) by embedding them into a reproducing kernel Hilbert space (RKHS) with a Gaussian kernel.[56] We empirically centered the Gram matrices by subtracting the row and column averages and adding the mean of the matrix elements. We then computed the test matrix by an element-wise multiplication of the three matrices (i.e., a Hadamard product) and averaging the matrix elements. To heuristically estimate the strength of the test statistic of the joint interaction, we normalized the test statistic value by the 95% confidence interval of the null distribution (i.e., the distribution of the test statistic values under the null hypothesis), computed using a Wild bootstrap permutation[57] to preserve the temporal dependency in the instantaneous phase data (we used at least 10,000 permutations, which we found to be stable in robustness tests). The resulting test statistic value approximates the joint high-order interaction (JHOI) between the three instantaneous phase traces, i.e., a higher JHOI corresponds to a stronger interaction between the phase traces.

To identify frequency quadruplet clusters with a group-level significance, we used a cluster permutation t test. We computed the t-value of each frequency quadruplet's JHOI (taking the median JHOI of each quadruplet's four frequency triplets) across the recordings using a pairwise t test against a null distribution generated from surrogate data. The surrogate data was generated from the recording time series by resetting the phase delay of its frequency components in the Fourier space. We then clustered frequency quadruplets with a p-value threshold of 0.01 against a null distribution of cluster t-value sum, generated by permuting the condition's label. See Figure S5 for a characterization of the JHOI computation strategy using synthetic data.

Synthetic data

To generate oscillatory signals, we followed the methodology described by Haufler et al.[15] Briefly, an interval was defined for the frequency and amplitude of each signal (normally +/− 1 Hz for a given frequency and 0.5–1 amplitude for a given signal). Using these intervals, a frequency vector and amplitude vector was generated using cubic spline interpolation at 0.8ms steps (negative values of frequency or amplitude were set to zero). Next, a phase variable was integrated over the signal, advanced at a rate proportional to the instantaneous frequency. The resulting phase was parsed to a cosine function to generate an oscillatory signal which is then scaled at each point in time by the instantaneous amplitude vector. Two oscillatory signals components were combined by their simple addition and via a non-linear activation function (here we used a quadratic function), $F(s) = B + Cs + Ds^2$, where $s = S_1 + S_2$ is comprised of two oscillatory signals and expansion of this result gives, $F(S_1 + S_2) = B + CS_1 + CS_2 + DS_1^2 + DS_2^2 + 2DS_1S_2$. Finally, white noise σ is added to the resulting signal.

Surrogate data

To generate surrogate data, we used the original time-series signal and shuffled the phase components.[58] We first performed a fast Fourier transform (MATLAB, fft function), take the absolute magnitude of the spectral density (MATLAB, abs function), and finally perform an inverse fast Fourier transform (MATLAB, ifft function). The surrogates retained (i) the spectral power distribution of each respective time-series but removed the phase relationships between frequency components and (ii) retained the temporal dependence necessary for comparative time-series. Note that this should not be confused with the generation of null distributions for the non-parametric test for Lancaster interaction.

Cluster permutation t test

The cluster-based permutation t test was used to identify significant frequency mixing quadruplets at the group-level using their JHOI values. We computed an uncorrected t test (paired or two-sample t-tests depending on data) for each quadruplet. We retained quadruples with p-value <0.01 and clustered them according to their similarity in terms of both their frequency difference and spatial distance. The similarity in frequency was defined such that for two quadruplets a and b, $(f_1^a, f_2^a, \Delta f^a, \sum f^a)$ and $(f_1^b, f_2^b, \Delta f^b, \sum f^b)$, if their distance $\sqrt[2]{(f_1^a - f_1^b)^2 + (f_2^a - f_2^b)^2 + (\Delta f^a - \Delta f^b)^2 + (\sum f^a - \sum f^b)^2} \leq 2$ the quadruplets were considered neighbors. The similarity in space was defined by the EEG electrode locations, such that two quadruplets were considered neighbors if at least three frequencies from one quadruplet were recorded from the same electrodes as the corresponding frequencies in the second quadruplet. For example, f_1^a and f_1^b recorded from the same electrode, f_2^a and f_2^b recorded from the same electrode, and $\sum f^a$ and $\sum f^b$ recorded from the same electrode. For each cluster, the t-values are summed and then compared against a null distribution. The null distribution was generated by permuting the condition label 50,000 times and then re-clustering and calculating the maximum cluster t-value sum for each permutation. The t-sum of each cluster in the original data was then contrasted with the null distribution and significant ($p < 0.05$) clusters are identified.

Statistical analysis

Values in text and supplementary tables are mean ± standard deviation (SD). Statistical tests are specified in text/figure legends/supplementary tables. All t-tests are two tailed unless stated. In all plots, the * notation represents a statistical significance that survived Bonferroni correction if required.